

Computational Approaches to
Understanding Surface Heat Flow, the
Metamorphic Rock Record, and Subduction
Geodynamics

by

Buchanan C. Kerswell

A dissertation

submitted in partial fulfillment

of the requirements for the degree of

Doctor of Philosophy in Geosciences

Boise State University

November 2021

© 2021

Buchanan C. Kerswell

ALL RIGHTS RESERVED

BOISE STATE UNIVERSITY GRADUATE COLLEGE

DEFENSE COMMITTEE AND FINAL READING APPROVALS

of the dissertation submitted by

Buchanan C. Kerswell

Dissertation Title: Computational Approaches to Understanding Surface Heat Flow, the Metamorphic Rock Record, and Subduction Geodynamics

Date of Final Oral Examination: August 27, 2021

The following individuals read and discussed the dissertation submitted by student Buchanan C. Kerswell, and they evaluated the student's presentation and response to questions during the final oral examination. They found that the student passed the final oral examination.

Matthew J. Kohn Ph.D.	Chair, Supervisory Committee
C.J. Northrup Ph.D.	Member, Supervisory Committee
H.P. Marshall Ph.D.	Member, Supervisory Committee
Philippe Agard Ph.D.	External Member, Supervisory Committee

The final reading approval of the dissertation was granted by Matthew J. Kohn Ph.D., Chair of the Supervisory Committee. The dissertation was approved by the Graduate College.

DEDICATION

To my mentors, colleagues, friends, and loved ones who take special interests in my life.

This work is yours as much as it is mine.

ACKNOWLEDGMENT

This work was only possible through the efforts of many individuals. My advisor, Dr. Matthew Kohn, deserves special recognition for his contributions, mentorship, and relentless support during the course of my studies. Dr. Taras Gerya and the Geophysical Fluid Dynamics group at the Institut für Geophysik, ETH Zürich, generously offered their high-performance computing resources from the Euler cluster, invaluable instruction, discussion, and support on the numerical modelling methods, and many free meals in Zürich. Additional high-performance computing support from the Borah cluster was provided by the Research Computing Department at Boise State University. Thanks to Dr. D. Hasterok for providing references and guidance on citing the large dataset in chapter three. Special thanks to Dr. Philippe Agard, Dr. Laetitia Le Pourhiet, and graduate students at Sorbonne Université for their incredible expertise and showing me the best of summertime Paris. Thanks to many anonymous reviewers, graduate students, and colleagues for helpful comments on technical aspects of each chapter. My deep appreciation of metamorphic rocks and Alpine geology was formed thanks to outstanding field excursions expertly guided by EFIRE and ZiP graduate students, faculty, and affiliates. Funding for this work was provided by the National Science Foundation grant OIA1545903 awarded to Dr. Matthew Kohn, Dr. Sarah

Penniston-Dorland, and Dr. Maureen Feineman. Datasets and code for reproducing this research are available at <https://github.com/buchanankerswell>.

ABSTRACT

Pressure-temperature-time (PTt) estimates from high-pressure (HP) metamorphic rocks and global surface heat flow (SHF) rates evidently encode information about pressure-temperature-strain (PTS) fields deep in subduction zones (SZs). Previous work demonstrates the possibility of decoding such geodynamic information by comparing physics-based numerical models with empirical observations of SHF and the metamorphic rock record. However, antithetical interpretations of (non)uniformity with respect to PTS fields are emerging from this line of inquiry. For example, while mechanical coupling depths (CDs) inverted from SHF are narrowly distributed among SZs, maximum pressure-temperature (PT) conditions inverted from exhumed metamorphic rocks are relatively wide-ranging, and yet also uniformly distributed across pressures up to 2.4 GPa. This dissertation scrutinizes (dis)similarities among SZs inferred from large numerical and empirical datasets by applying a variety of computational techniques. First, CDs for 13 modern SZs are predicted after observing coupling in 64 numerical geodynamic simulations. Second, spatial patterns of SHF are assessed in two-dimensions by interpolating thousands of SHF observations near several SZ segments. Third, PTt distributions of over one million markers traced from the previous set of 64 SZ simulations are compared with hundreds of empirical PTt estimates

from the rock record to assess the effects of thermo-kinematic boundary conditions (TKBCs) on deep mechanical processing of rock in SZs. These studies conclude the following. Mechanical coupling between plates is primarily controlled by the upper plate lithospheric thickness, with marginal responses to other TKBCs. SHF interpolations show high variance within and among SZ segments, suggesting local, rather than widespread, continuity of PTS fields deep within SZs. Computed marker recovery rates correlate with TKBCs, and are therefore expected to vary among SZs. Finally, computed PTt distributions of markers show patterns consistent with transient, localized recovery from a cooling, serpentinizing plate interface. Together, this work encourages more antireductionist and diversified views of subduction geodynamics until SHF and PTt datasets can more precisely distinguish (dis)similarities in PTS fields within and among SZs. Strategically scaling PTt and SHF datasets in the future will improve computational precision and confidence, and thus will advance subduction zone research.

TABLE OF CONTENTS

Dedication	iv
Acknowledgment	v
Abstract	vii
List of Figures	xi
List of Tables	xii
List of Abbreviations	xiii
List of Symbols	xiv
1 Introduction	1
2 Effects of Thermo-kinetic Boundary Conditions on Mechanical Plate Coupling in Subduction Zones	3
2.1 Abstract	3
2.2 Introduction	4
2.3 Numerical modelling methods	7
2.3.1 Initial setup and boundary conditions	8
2.3.2 Calculating geotherms and defining lithospheric thickness	11

3	A Comparison of Heat Flow Interpolations Near Subduction Zones	15
3.1	Abstract	15
	References	17

LIST OF FIGURES

2.1 Initial model configuration and boundary conditions 10

2.2 Range of key thermo-kinematic boundary conditions used in numerical
experiments 12

LIST OF TABLES

2.1	Rheologic parameters used in numerical experiments	9
2.2	Melting curve constants used in numerical experiments	9

LIST OF ABBREVIATIONS

CD coupling depth

HP high-pressure

PT pressure-temperature

PTS pressure-temperature-strain

PTt pressure-temperature-time

SHF surface heat flow

SZ subduction zone

TKBCs thermo-kinematic boundary conditions

UPT upper plate thickness

LIST OF SYMBOLS

GPa Gigapascal

K Kelvin

Ma *Mega annum* or million-years

Z_{UP} Upper plate thickness

Z_{cpl} Mechanical coupling depth

Φ Thermal parameter

η viscosity

\vec{q} surface heat flow

\vec{v}_{conv} convergence velocity

$^{\circ}C$ Celcius

km kilometer

t_{OP} oceanic plate age

CHAPTER 1:

INTRODUCTION

Keypoints:

- Proxy datasets are key for inference about geodynamics deep in **SZs**
- Computation leverages large data to infer, build, and test geodynamic models

CHAPTER 2:

EFFECTS OF THERMO-KINETIC BOUNDARY CONDITIONS ON MECHANICAL PLATE COUPLING IN SUBDUCTION ZONES

Keypoints:

- Mechanical coupling responds strongly to **upper plate thickness (UPT)**
- Inverting **surface heat flow (SHF)** allows **coupling depth (CD)** estimation
- Globally consistent **UPT** would imply globally uniform **CDs**

2.1 Abstract

Deep mechanical coupling between converging plates is implicated in seismic cycles, arc magmatism, and considered a key feature of **subduction zone (SZ)** geodynamics. This study uses two-dimensional numerical models of oceanic-continental convergent margins

to investigate effects of **thermo-kinematic boundary conditions (TKBCs)** on coupling—specifically focusing on thermal parameter (Φ) and **upper plate thickness (UPT)**. The numerical experiments implement coupling by including antigorite (de)stabilization in the mantle wedge. Experiments show thermal feedbacks regulating **coupling depth (CD)** self-consistently with strong responses to **UPT** and weak responses to Φ . The results imply estimation of **CD** is possible by inverting **UPT** from **surface heat flow (SHF)**. **SHF** sampled from 13 modern **SZs** suggest uniform **UPT** and therefore consistent **CDs** among **SZs**.

2.2 Introduction

Subduction geodynamics strongly depend on the depth where a subducting plate and overlying mantle wedge transition from mechanically decoupled (moving differentially with respect to each other) to mechanically coupled (moving with the same local velocity, [Furukawa, 1993](#); [Peacock *et al.*, 1994](#); [Wada *et al.*, 2008](#)). For example, traction forces driving mantle wedge circulation at the (de)coupling transition define a rapid increase in temperature along the top of the subducting plate ([Peacock, 1996](#)). Many observations from numerical experiments and **SHF** infer **CDs** occurring globally at 70-80 *km* in modern **SZs**, essentially independent of other **TKBCs** including oceanic-plate age (t_{OP}), convergence velocity (\vec{v}_{conv}), and subduction geometry ([Furukawa, 1993](#); [Wada *et al.*, 2008](#); [Wada & Wang, 2009](#)). To understand **SZ** geodynamics, it is important to understand why modern subduction zones appear to achieve similar depths of coupling despite differences in physical characteristics.

Notwithstanding, many numerical geodynamic models use **CDs** of 70-80 *km* as a bound-

ary condition (e.g., [Abers *et al.*, 2017](#); [Currie *et al.*, 2004](#); [Syracuse *et al.*, 2010](#); [van Keken *et al.*, 2011, 2018](#); [Wada *et al.*, 2012](#); [Gao & Wang, 2014](#); [Wilson *et al.*, 2014](#)), although not exclusively (e.g. 40-56 *km*, [England & Katz, 2010](#); [Peacock, 1996](#)). Similar **CDs** among **SZs** is an attractive hypothesis for at least two reasons. First, it helps explain a relatively narrow range of depths to subducting oceanic-plates beneath volcanic arcs ([England *et al.*, 2004](#); [Syracuse & Abers, 2006](#)) because mechanical coupling is expected to be closely associated with the onset of flux melting. Second, mechanical coupling is required to detach and recover rocks from the subducting plate ([Agard *et al.*, 2016](#)), so a common depth of coupling may also help explain why maximum pressures recorded by subducted oceanic material worldwide is $\leq 2.3\text{-}2.5$ *GPa* (roughly 80 *km*, [Agard *et al.*, 2009, 2018](#)).

The location and extent of mechanical coupling along the plate interface is implicated in myriad geodynamic phenomena (seismicity, metamorphism, volatile fluxes into the mantle wedge, volcanism, and plate motions, e.g., [Čížková & Bina, 2013](#); [Gonzalez *et al.*, 2016](#); [Peacock, 1990, 1991, 1993, 1996](#); [Peacock & Hyndman, 1999](#); [Hacker *et al.*, 2003](#); [van Keken *et al.*, 2011](#); [Grove *et al.*, 2012](#); [Gao & Wang, 2017](#)). Consequently, the mechanics of coupling have been extensively studied and discussed. Coupling fundamentally depends on the strength (η ; viscosity) of materials above, within, and below the plate interface. Increasing **PT** and high water fluxes from compaction and dehydration of hydrous minerals form layers of low viscosity sheet silicates in the shallow forearc mantle wedge—especially talc and serpentine—inhibiting transmission of shear stress between plates ([Peacock &](#)

Hyndman, 1999). The lack of traction along the interface, combined with cooling from the subducting plate surface, ensures a cold and rigid forearc mantle. Experimentally determined flow laws, petrologic observations, and geophysical observations all support the plausibility of this conceptual model of subduction interface behaviour (e.g., Agard *et al.*, 2016, 2018; Gao & Wang, 2014; Peacock & Hyndman, 1999).

Two-dimensional numerical geodynamic models of subduction are key to investigating potential correlations between **CD**, **UPT** (inverted from backarc heat flow), and Φ . Wada & Wang (2009) previously investigated steady-state **CDs** by numerically modelling 17 active subduction zones. Among other **TKBCs**, their models specify convergence rate, subduction geometry, thermal structure of oceanic- and overriding-plates, and degree of coupling along the subduction interface. Their experiments control for interface rheology and discriminate the best-fit depth based on observed fore-arc heat flow.

In the present study, similar **TKBCs** are specified to simulate the range of modern **SZ** systems. However, subduction dip angle and, most importantly, interface rheology are regulated self-consistently by evolving **PTS** fields in a deforming mantle wedge. In other words, **CD** is not a fully determined feature, but rather a spontaneous model outcome within the range of specified boundary conditions discussed later. As in other previous studies (e.g., Ruh *et al.*, 2015), rheological effects of the dehydration reaction *antigorite* \Leftrightarrow *olivine* + *orthopyroxene* + H_2O are included to drive mechanical coupling by an abrupt viscosity increase with antigorite destabilization. The position of this reaction along the

subduction interface determines the **CD**.

This chapter focuses on two fundamental questions. How does **CD** respond to **TKBCs** (specifically Φ and **UPT**)? And how stable is **CD** through time? First, 64 convergent margins with variable **UPT** and Φ are numerically simulated and mechanical plate coupling is observed. Thermal feedbacks within the system are visualized in terms of mantle temperature, viscosity, and velocity fields. Most importantly, **CD** responses to a range of Φ and **UPT** are quantified using multi-variate linear regression. **CDs** are then predicted for 13 modern **SZs** using regressed models of three different forms. Implications and questions about **UPT** and **CD** uniformity among **SZs** are finally discussed before further investigation into **SHF** in Chapter 3.

2.3 Numerical modelling methods

The numerical experiments in this study simulate converging oceanic-continental plates, where an ocean basin is being consumed by subduction at a continental margin (Figure 2.1). The initial conditions are modified from previous numerical experiments of active margins (code: I2VIS, [Sizova et al., 2010](#); [Gorczyk et al., 2007](#)), although plate coupling was not the focus of their studies. Identical material properties (Tables 2.1 & 2.2), rheologic model, and hydration/melt model (see !!!Appendix) as [Sizova et al. \(2010\)](#) are used. However, the version of I2VIS in this study differs from [Sizova et al. \(2010\)](#) in its initial setup, overall dimension, resolution, continental geotherm, dehydration model, and left boundary condition (origin of new oceanic lithosphere). These differences are outlined below. Sixty-four models

were constructed with varying convergence rate (\vec{v}_{conv}), oceanic-plate age (t_{OP}), and the **UPT** (Figure 2.2).

2.3.1 Initial setup and boundary conditions

The two-dimensional model is 2000 *km* wide and 300 *km* deep (Figure 2.1). In the model domain, three governing equations of heat transport, motion, and continuity are discretized and solved using a conservative finite-difference with marker-in-cell approach on a fully staggered grid as outlined in Gerya & Yuen (2003). The model resolution is non-uniform with higher resolution (1 *km* x 1 *km*) in a 600 *km* wide area surrounding the contact between the ocean basin and continental margin, then gradually changing to lower resolution towards the model boundaries (5 *km* x 1 *km*, x- and z-directions, respectively). The left and right boundaries are free-slip and thermally insulating (Figure 2.1a, b). The implementation of “sticky” air and water allows for a free topographical surface with a simple linear sedimentation and erosion model. The lower boundary is open to allow for spontaneous oceanic-plate descent and subduction angle (Burg & Gerya, 2005).

Table 2.1: Rheologic parameters used in numerical experiments

Material	Flow Law	h	m	n	A	A_{diff}	A_{disl}	V	V_{diff}	V_{disl}	E	E_{diff}	E_{disl}	σ_{cr}	C	μ_0	μ_1
		[m]			[Pa ⁿ s]	[s ⁻¹]	[s ⁻¹]	[$\frac{J}{Pa \cdot mol}$]	[$\frac{J}{Pa \cdot mol}$]	[$\frac{J}{Pa \cdot mol}$]	[$\frac{J}{mol}$]	[$\frac{J}{mol}$]	[$\frac{J}{mol}$]	[Pa]	[Pa]		
Felsic sediments	Wet quartzite			2.3	1.97e+17			0.000003			154000			30000	1000000	0.2	0.1
Felsic crust	Wet quartzite			2.3	1.97e+17			0.000003			154000			30000	1000000	0.6	0.3
Oceanic crust	Plag An ₇₅			3.2	4.8e+22			0.000008			238000			30000	300000	0.6	0.2
Dry mantle	Dry olivine	0.001	2.5	3.5		8.7e+15	3.5e+22		0.000004	0.00002		300000	540000		1000000	0.6	0.3
Hydrated mantle	Wet olivine	0.001	2.5	3		5.3e+15	2e+18		0.000004	0.00001		240000	430000		1000000	0.6	0.3
Serpentinized mantle	Serpentine			3.8	3.21e+36			0.0000032			8900			3000000	1000000	0.2	0.1
Reference ¹	b, c, d	d	d	b, c, d	b, c	d	d	b, c	d	d	b, c	d	d	b, c	a		

h =grain size, m =grain size exponent, n =stress exponent, A =material constant, V =activation volume, E =activation energy, σ_{cr} =critical stress for dislocation creep, C =compressive strength at $P=0$, $\mu_{0,1}$ =initial and final internal friction coefficient, $\mu_0 = \mu_1 = 0$ for melt-bearing rocks

¹ a=Turcotte & Schubert (2002), b=Ranalli (1995), c=Hilaret et al. (2007), d=Karato & Wu (1993)

Table 2.2: Melting curve constants used in numerical experiments

Material	a^1	b^1	c^1	d^1	e^1	f^2	g^2	h^2	i^3	j^3
	[MPa]	[K]	[MPa]	[MPa]	[MPa] ²	[K]	[MPa] ⁻¹	[MPa] ⁻²	[K]	[MPa] ⁻¹
Felsic sediments	1200	889	17900	54	20200	831	0.0600		1262	0.009
Felsic crust	1200	889	17900	54	20200	831	0.0600		1262	0.009
Oceanic Crust	1600	973	704000	354	77800000	935	0.0035	0.000062	1423	0.105
Dry mantle						1394	0.1330	-0.000051	2073	0.114
Hydrated mantle	2400	1240	49800	323			127000.0000	0.000035	2073	0.114
Serpentinized mantle	2400	1240	49800	323			127000.0000	0.000035	2073	0.114

After phase diagrams from Schmidt & Poli (1998)

$$^1 T_{solidus}(P) = b + \frac{c}{(P+d)} + \frac{e}{(P+d)^2} \text{ at } P < a$$

$$^2 T_{solidus}(P) = f + gP + hP^2 \text{ at } P \geq a$$

$$^3 T_{liquidus}(P) = i + jP$$

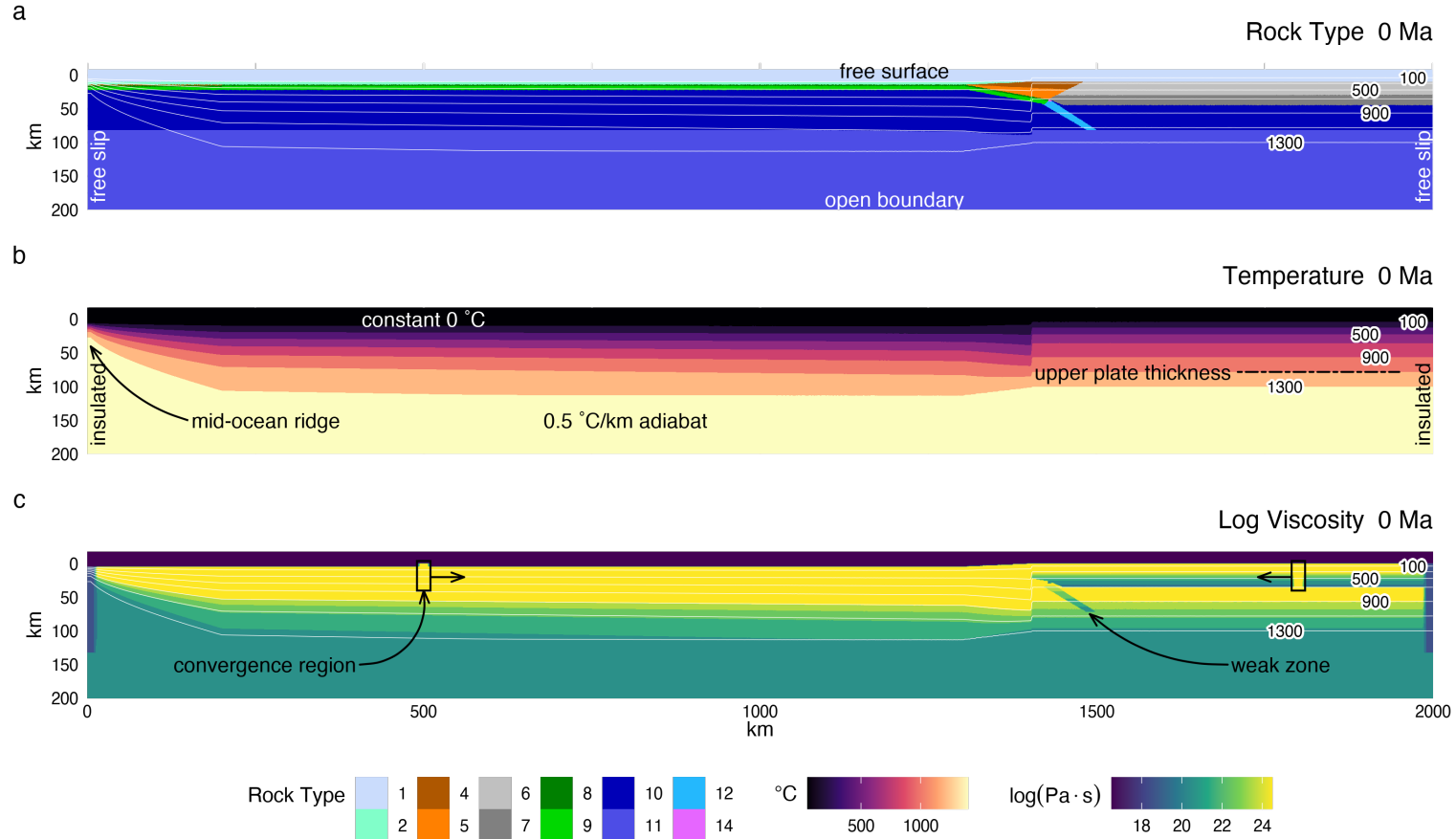


Figure 2.1: Initial model configuration and boundary conditions. (a) A free sedimentation/erosion boundary at the surface is maintained by implementing a layer of "sticky" air and water, and an infinite-like open boundary at the bottom allows for spontaneous oceanic-plate descent and subduction angle. The left and right boundaries are free slip and insulating. The initial material distribution includes 7 km of oceanic crust (2 km basalt, 5 km gabbro), 1 km of oceanic sediments, and 35 km of continental crust, thinning ocean-ward. (b) Oceanic lithosphere is continually created at the left boundary. The oceanic geotherm is calculated using a half-space cooling model and the continental geotherm is calculated using a one-dimensional steady-state conductive cooling model to 1300 °C. The base of the mechanical lithosphere (Z_{UP}) is defined by visualizing viscosity and generally coincides with the 1100 °C isotherm. (c) The oceanic crust is bent under loading from passive margin sediments, and a weak zone extends from the deflected oceanic crust, through the lithosphere, to help induce subduction. Convergence velocities are imposed at stationary, high-viscosity regions far from the trench. Rock type colors are: [1] air, [2] water, [4,5] sediments, [6,7] felsic crust, [8] basalt, [9] gabbro, [10,11] dry mantle, [12] hydrated mantle, [14] serpentinized mantle.

A horizontal convergence force is applied to both plates in a rectangular region far from the continental margin (Figure 2.1c). An initial weak layer cutting the lithosphere permits subduction to initiate. The high-viscosity ($\eta = 10^{25} \text{ Pa} \cdot \text{s}$) rectangular convergence regions apply constant horizontal velocities without deforming the lithosphere. The subduction angle is governed by the free-motion of the subducting plate. Similarly, subduction velocity can vary with time in response to extension or shortening of the overriding plate. Therefore, the thermal parameter (Φ) is calculated in this study as the product of the horizontal convergence velocity (\vec{v}_{conv}) and the oceanic-plate age (t_{OP} , c.f. McKenzie, 1969). For convenience and consistency with the literature, this study presents Φ as $\Phi/100$ (Figure 2.2a).

2.3.2 Calculating geotherms and defining lithospheric thickness

The oceanic crust is modeled as 1 km of sediment cover overlying 2 km of basalt and 5 km of gabbro (Figure 2.1a). Oceanic lithosphere is continually made at a pseudo-mid-ocean ridge at the left boundary of the model (Figure 2.1b). An enhanced vertical cooling condition is applied at 200 km from left boundary to adjust for the proper oceanic-plate age, and therefore its lithospheric thickness as it enters the trench (Agrusta *et al.*, 2013). Plate ages from 32.6 to 110 Ma and convergence velocities from 40 to 100 km/Ma are used in this study (Figure 2.2a). This range of parameters broadly reflects the middle-range of the modern global subduction system (Syracuse & Abers, 2006).

Initial continental geotherms are determined by solving the heat flow equation in one-dimension to 1300 °C (Figure 2.2b). This study assumes a fixed temperature of 0 °C at

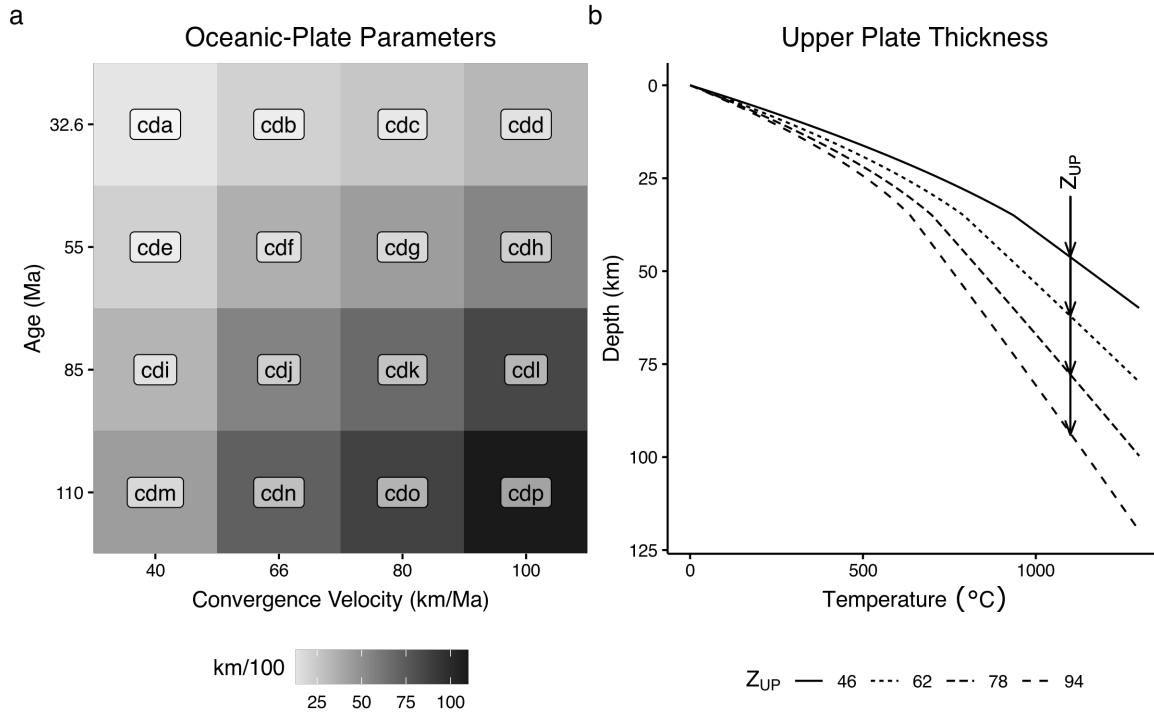


Figure 2.2: Range of key thermo-kinematic boundary conditions used in numerical experiments. (a) Modelled thermal parameters (grayscale) range from 13 to 110 $km/100$ and broadly reflect the distribution of oceanic-plate ages and convergence velocities in modern subduction zones. Model names include the prefix "cd" for "coupling depth" with increasing alphabetic suffixes. Note that neither axes are continuous. (b) Upper plate thickness (Z_{UP}) is defined by a range of continental geotherms. Geotherms were constructed using a one-dimensional steady-state conductive cooling model with $T(z=0) = 0^\circ C$ and $\vec{q}(z=0) = 59, 63, 69, 79 mW/m^2$, and constant radiogenic heating of $1.0 \mu W/m^3$ for a 35 km-thick crust and $0.022 \mu W/m^3$ for the mantle. The continental geotherms are calculated up to $1300^\circ C$, with a $0.5^\circ C/km$ gradient (the mantle adiabat) for higher temperatures.

the surface, constant radiogenic heating of $1 \mu\text{W}/\text{m}^3$ in the 35 km-thick continental crust, $0.022 \mu\text{W}/\text{m}^3$ in the mantle, with thermal conductivities of $2.3 \text{ W}/\text{mK}$ and $3.0 \text{ W}/\text{mK}$ for the continental crust and mantle, respectively. Above, 1300°C , temperature is assumed to increase by $0.5^\circ\text{C}/\text{km}$ (the mantle adiabat).

Many studies define the base of the continental lithosphere at the 1300°C isotherm, but it can be determined directly by visualizing viscosity and strain rate as the model progresses. The mechanical base of the lithosphere (Z_{UP}) in the models generally occurs at the 1100°C isotherm—characterized by a rapid decrease in viscosity and increase in strain rate (Figures ??, ??, ??). As such, this study considers the oceanic and continental lithosphere as mechanical layers defined by viscosity, rather than defined merely by temperature. The range of Z_{UP} corresponds to backarc surface heat flow of 59, 63, 69, and $79 \text{ mW}/\text{m}^2$.

CHAPTER 3:

A COMPARISON OF HEAT FLOW INTERPOLATIONS NEAR SUBDUCTION ZONES

Keypoints:

- Inconsistent spatial patterns characterize heat flow near subduction zones
- Heat flow investigations favour 2D interpolations over 1D transects
- Scaling datasets and new interpolation schema will advance **SZ** research

3.1 Abstract

Heat fluxing through the Earth's surface provides indirect observations of **pressure-temperature-strain (PTS)** fields deep in **SZs**. Global heat flow databases, therefore, are invaluable for generating and testing belief about **SZ** geodynamics. Investigating **surface heat flow (SHF)** in two-dimensions by interpolation, rather than in one-dimension by

projection, arguably forms better interpretations about spatial continuity of deep processes. Direct comparisons of interpolations based on the First (spatial continuity) and Third (similarity) Laws of Geography applied to the most updated global heat flow database. Inconsistent spatial patterns of SHF near SZs are observed in magnitude and variance, regardless of interpolation method. The implications include discontinuous PTS fields at depth, countering hypotheses of commonly thin upper plate lithospheres and mechanical CDs among subduction zones. Strategic scaling of SHF datasets will improve interpolation precision and confidence—leading to better tools for distinguishing differences within and among SZs. New data acquisition and composite interpolation schema are proposed as avenues for future SZ research.

REFERENCES

- Abers, G. A., van Keken, P. E., & Hacker, B. R. 2017. The cold and relatively dry nature of mantle forearcs in subduction zones. *Nature Geoscience*, **10**(5), 333–337.
- Agard, P., Yamato, P., Jolivet, L., & Burov, E. 2009. Exhumation of oceanic blueschists and eclogites in subduction zones: Timing and mechanisms. *Earth-Science Reviews*, **92**(1-2), 53–79.
- Agard, P., Yamato, P., Soret, M., Prigent, C., Guillot, S., Plunder, A., Dubacq, B., Chauvet, A., & Monié, P. 2016. Plate interface rheological switches during subduction infancy: Control on slab penetration and metamorphic sole formation. *Earth and Planetary Science Letters*, **451**, 208–220.
- Agard, P., Plunder, A., Angiboust, S., Bonnet, G., & Ruh, J. B. 2018. The subduction plate interface: Rock record and mechanical coupling (from long to short time scales). *Lithos*, **320-321**, 537–566.
- Agrusta, R., Arcay, D., Tommasi, A., Davaille, A., Ribe, N., & Gerya, T. 2013. Small-scale convection in a plume-fed low-viscosity layer beneath a moving plate. *Geophysical Journal International*, **194**(2), 591–610.

- Burg, J. P., & Gerya, T. 2005. The role of viscous heating in Barrovian metamorphism of collisional orogens: thermomechanical models and application to the Lepontine Dome in the Central Alps. *Journal of Metamorphic Geology*, **23**(2), 75–95.
- Čížková, H., & Bina, C. R. 2013. Effects of mantle and subduction-interface rheologies on slab stagnation and trench rollback. *Earth and Planetary Science Letters*, **379**, 95–103.
- Currie, C. A., Wang, K., Hyndman, R. D., & He, J. 2004. The thermal effects of steady-state slab-driven mantle flow above a subducting plate: The Cascadia subduction zone and backarc. *Earth and Planetary Science Letters*, **223**(1-2), 35–48.
- England, P., & Katz, R. F. 2010. Melting above the anhydrous solidus controls the location of volcanic arcs. *Nature*, **467**(7316), 700–703.
- England, P., Engdahl, R., & Thatcher, W. 2004. Systematic variation in the depths of slabs beneath arc volcanoes. *Geophysical Journal International*, **156**(2), 377–408.
- Furukawa, Y. 1993. Magmatic Processes Under Arcs and Formation of the Volcanic Front. *Journal of Geophysical Research*, **98**, 8309–8319.
- Gao, X., & Wang, K. 2014. Strength of stick-slip and creeping subduction megathrusts from heat flow observations. *Science*, **345**(6200), 1038–1041.
- Gao, X., & Wang, K. 2017. Rheological separation of the megathrust seismogenic zone and episodic tremor and slip. *Nature*, **543**(7645), 416–419.

- Gerya, T., & Yuen, D. A. 2003. Characteristics-based marker-in-cell method with conservative finite-differences schemes for modeling geological flows with strongly variable transport properties. *Physics of the Earth and Planetary Interiors*, **140**(4), 293–318.
- Gonzalez, Christopher M, Gorczyk, Weronika, & Gerya, TV. 2016. Decarbonation of subducting slabs: Insight from petrological–thermomechanical modeling. *Gondwana Research*, **36**, 314–332.
- Gorczyk, W., Willner, A. P., Gerya, T., Connolly, J. A.D., & Burg, J. P. 2007. Physical controls of magmatic productivity at Pacific-type convergent margins: Numerical modelling. *Physics of the Earth and Planetary Interiors*, **163**(1-4), 209–232.
- Grove, T. L., Till, C. B., & Krawczynski, M. J. 2012. The Role of H₂O in Subduction Zone Magmatism. *Annual Review of Earth and Planetary Sciences*, **40**(1), 413–439.
- Hacker, B. R., Peacock, S. M., Abers, G. A., & Holloway, S. D. 2003. Subduction factory 2. Are intermediate-depth earthquakes in subducting slabs linked to metamorphic dehydration reactions? *Journal of Geophysical Research: Solid Earth*, **108**(B1).
- McKenzie, D. P. 1969. Speculations on the Consequences and Causes of Plate Motions. *Geophysical Journal International*, **18**(1), 1–32.
- Peacock, S. M. 1990. Fluid processes in subduction zones. *Science*, **248**(4953), 329–337.
- Peacock, S. M. 1991. Numerical simulation of subduction zone pressure-temperature-time

- paths: constraints on fluid production and arc magmatism. *Philosophical Transactions of the Royal Society of London. Series A: Physical and Engineering Sciences*, **335**(1638), 341–353.
- Peacock, S. M. 1993. The importance of blueschist → eclogite dehydration reactions in subducting oceanic crust. *Geological Society of America Bulletin*, **105**(5), 684–694.
- Peacock, S. M. 1996. Thermal and petrologic structure of subduction zones. *Subduction: top to bottom*, **96**, 119–133.
- Peacock, S. M., & Hyndman, R. D. 1999. Hydrous minerals in the mantle wedge and the maximum depth of subduction thrust earthquakes. *Geophysical Research Letters*, **26**(No. 16), 2517–2520.
- Peacock, S. M., Rushmer, T., & Thompson, A. B. 1994. Partial melting of subducting oceanic crust. *Earth and planetary science letters*, **121**(1-2), 227–244.
- Ruh, J. B., Le Pourhiet, L., Agard, P., Burov, E., & Gerya, T. 2015. Tectonic slicing of subducting oceanic crust along plate interfaces: Numerical modeling. *Geochemistry, Geophysics, Geosystems*, **16**(10), 3505–3531.
- Sizova, E., Gerya, T., Brown, M., & Perchuk, L. L. 2010. Subduction styles in the Precambrian: Insight from numerical experiments. *Lithos*, **116**(3-4), 209–229.

- Syracuse, E. M., & Abers, G. A. 2006. Global compilation of variations in slab depth beneath arc volcanoes and implications. *Geochemistry, Geophysics, Geosystems*, **7**(5).
- Syracuse, E. M., van Keken, P. E., Abers, G. A., Suetsugu, D., Bina, C. R., Inoue, T., Wiens, D., & Jellinek, M. 2010. The global range of subduction zone thermal models. *Physics of the Earth and Planetary Interiors*, **183**(1-2), 73–90.
- van Keken, P. E., Hacker, B. R., Syracuse, E. M., & Abers, G. A. 2011. Subduction factory: 4. Depth-dependent flux of H₂O from subducting slabs worldwide. *Journal of Geophysical Research*, **116**(B1), B01401.
- van Keken, P. E., Wada, I., Abers, G. A., Hacker, B. R., & Wang, K. 2018. Mafic High-Pressure Rocks Are Preferentially Exhumed From Warm Subduction Settings. *Geochemistry, Geophysics, Geosystems*, **19**(9), 2934–2961.
- Wada, I., & Wang, K. 2009. Common depth of slab-mantle decoupling: Reconciling diversity and uniformity of subduction zones. *Geochemistry, Geophysics, Geosystems*, **10**(10), n/a–n/a.
- Wada, I., Wang, K., He, J., & Hyndman, R. D. 2008. Weakening of the subduction interface and its effects on surface heat flow, slab dehydration, and mantle wedge serpentinization. *Journal of Geophysical Research: Solid Earth*, **113**(4), 1–15.
- Wada, I., Behn, M. D., & Shaw, A. M. 2012. Effects of heterogeneous hydration in the

incoming plate, slab rehydration, and mantle wedge hydration on slab-derived H₂O flux in subduction zones. *Earth and Planetary Science Letters*, **353-354**, 60–71.

Wilson, C. R., Spiegelman, M., van Keken, P. E., & Hacker, B. R. 2014. Fluid flow in subduction zones: The role of solid rheology and compaction pressure. *Earth and Planetary Science Letters*, **401**, 261–274.